Science Advances
AAAS

Supplementary Materials for

All-optical graph representation learning using integrated diffractive photonic computing units

Tao Yan *et al.*

Corresponding author: Xing Lin, lin-x@tsinghua.edu.cn; Hongkai Xiong, xionghongkai@sjtu.edu.cn; Qionghai Dai, daiqh@tsinghua.edu.cn

Sci. Adv. **8**, eabn7630 (2022)
DOI: 10.1126/sciadv.abn7630

This PDF file includes:

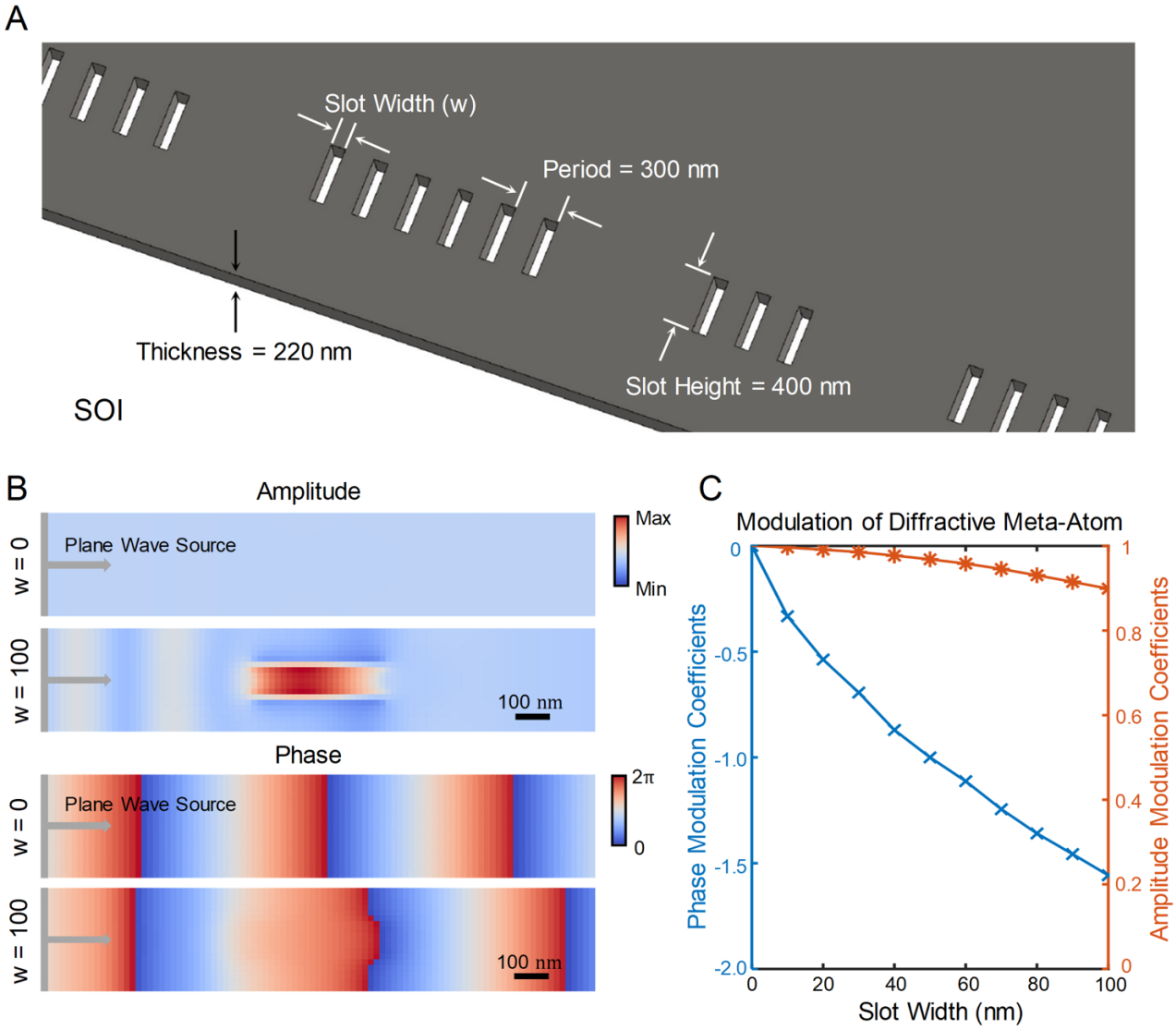

Figure S1. Modulation of optical field using diffractive meta-atoms. (A) A schematic view of metaline composed of diffractive meta-atoms, which are the 1D rectangular silica slot arrays etched on silicon-on-insulator (SOI) substrate. The thickness of the silicon membrane of SOI is 220 nm, and the height of the slot is 400 nm. The period of the diffractive meta-atom is 300 nm. The amplitude and phase modulations of optical fields are controlled by varying the slot width. (B) Comparison of the electric field distribution between free propagation of light in SOI substrate (the first and third lines) and that modulated by a silica slot with 100 nm wide (the second and fourth lines). The electric field distribution is obtained via FDTD numerical evaluation. (C) The phase and amplitude modulation coefficients of a diffractive meta-atom with respect to the slot width.

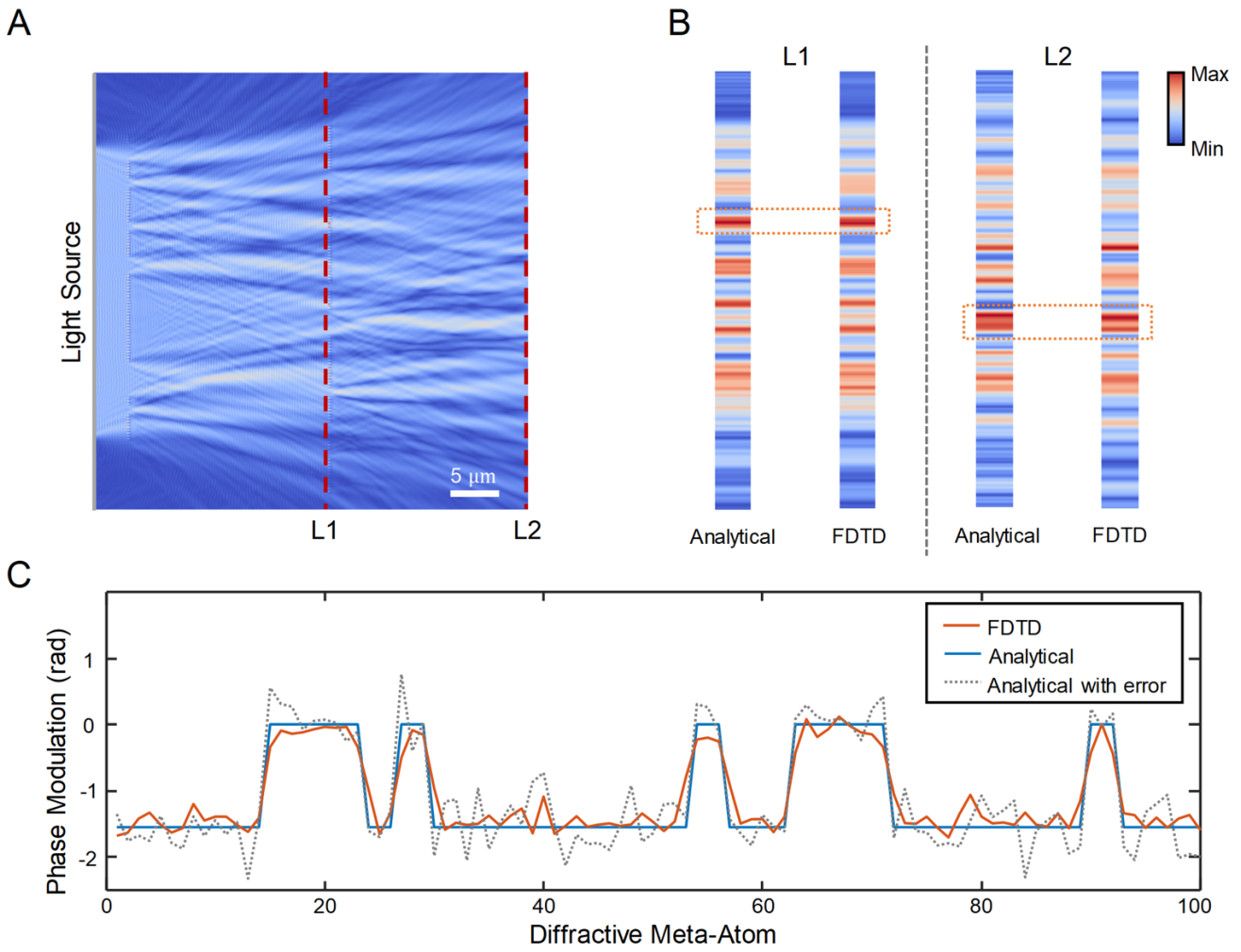

Figure S2. Evaluation of the analytical model accuracy using photonic finite-difference time-domain (FDTD). (A) The input light source for the module is a plane optical wave with an amplitude of 1, which is modulated by two metalines that are evaluated by using FDTD. Each metaline is configured with 150 binary diffractive meta-atoms, in which every consecutive 3 meta-atoms are set to have the same modulation. With a size of 300 nm for each meta-atom, the length of metaline is 45 μm. The distance of metaline layers is set to be 20 μm, and the optical fields at positions of L1 and L2 are monitored. (B) Comparisons of the intensity of optical fields at the position of L1 and L2 between the analytical and FDTD evaluations. (C) The phase modulation coefficients obtained by the FDTD evaluation (orange plot) with comparisons to the analytical model (blue plot) and analytical model with Gaussian noise (standard deviation of 0.3, dash line). The result shows the highly-matched output optical fields and phase modulation of the analytical model with respect to FDTD evaluation, where the residual errors can be further modeled by including Gaussian noise for high-accuracy analytical evaluation.

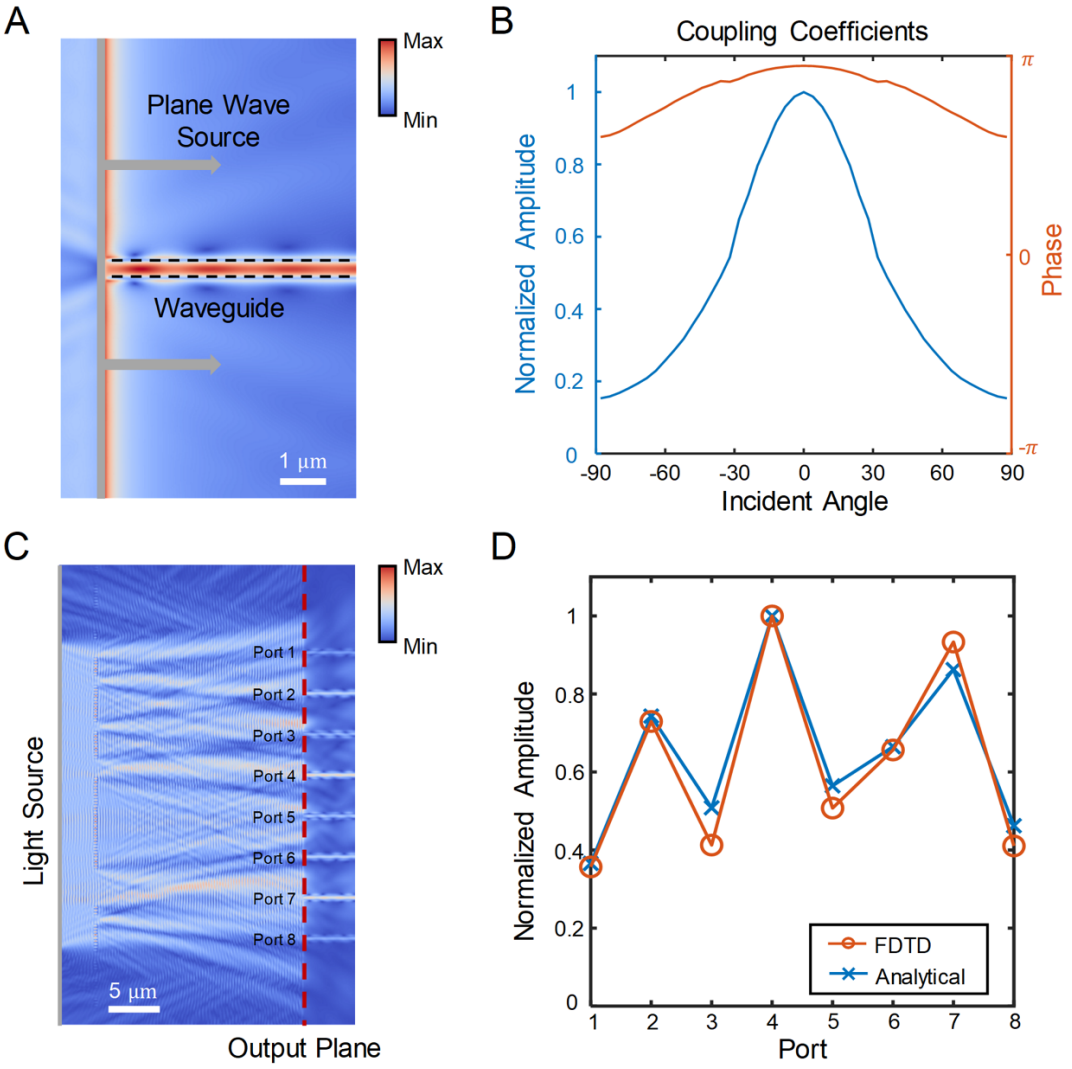

Figure S3. Evaluation of the output waveguide coupling. The analytical modeling of each output waveguide is obtained by first computing the Fast Fourier Transform (FFT) of the optical field at the output plane, where each Fourier component represents an incident light angle. Second, the coupling coefficients between the output waveguide and different incident light angles are obtained by using FDTD, where the 180° angle is divided into 45 parts and the coupling coefficient of each part is assumed to be the same. Third, the complex value of the output waveguide is computed by the weighted sum of the FFT values with respect to their corresponding coupling coefficients. (A) The electric field coupling between the incident plane wave and an output waveguide evaluated with FDTD. (B) The normalized coupling coefficients with respect to the incident light angles obtained via FDTD, forming as a Gaussian profile. (C) The electric field of the light source being modulated, propagated, and coupled to eight output waveguides. (D) The comparison of the amplitude of waveguide outputs between FDTD and analytical evaluations.

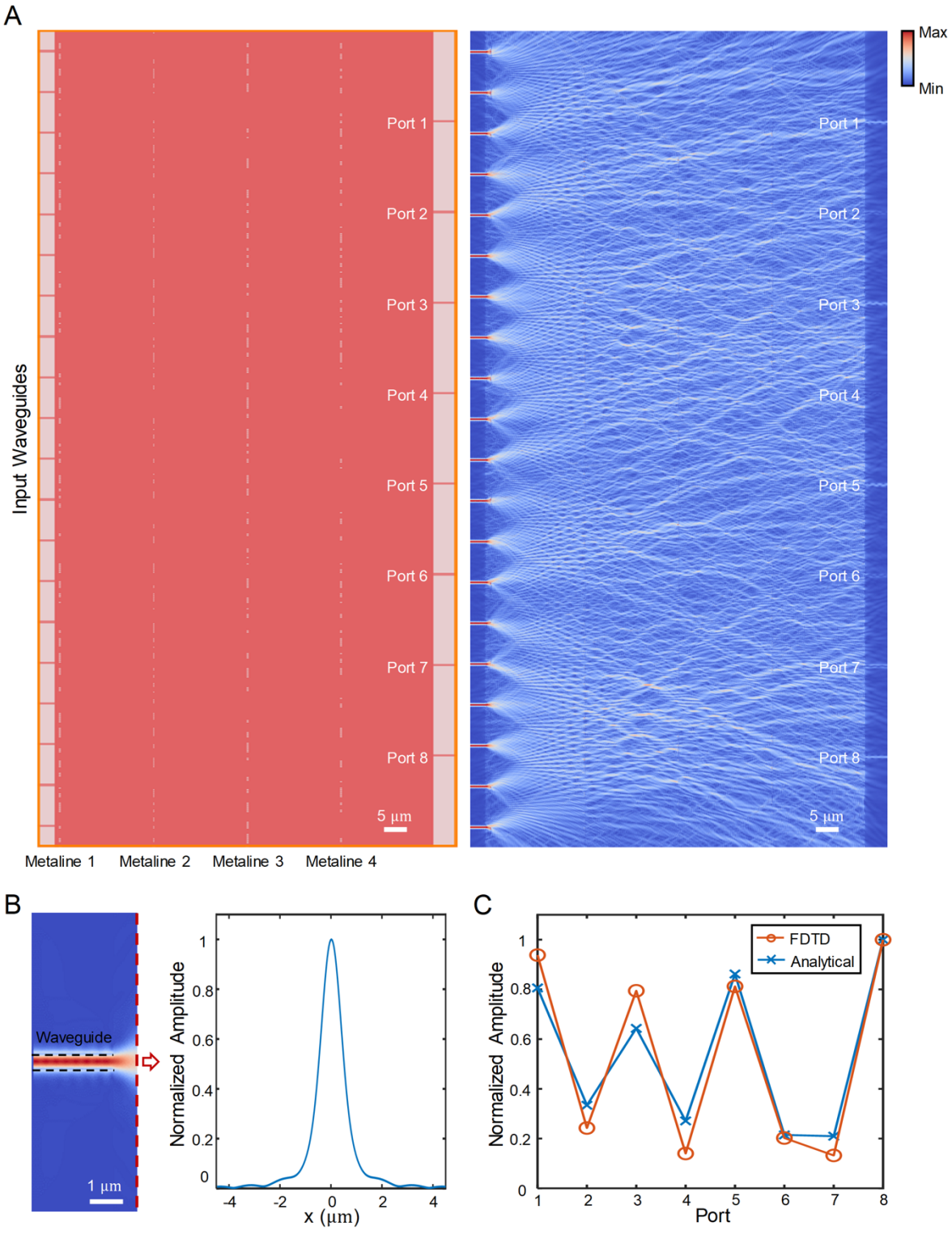

Figure S4. Evaluation of DPU computational results. (A) The DPU structure with 20 input and 8 output waveguides and the electric field propagation obtained with FDTD, where the distance between every two

successive layers is 20 μm. (B) The electric field coupling between the input waveguide and the first diffractive layer. In analytical modeling, the complex value of every input waveguide is multiplied by the coupling coefficients obtained via FDTD to obtain its electric field at the input plane with a 9 μm diameter region, where the amplitude values exhibit a Gaussian profile. (C) The comparison of the amplitude of 8 output waveguides between the analytical and FDTD evaluation, which demonstrates the effectiveness of using the analytical model for designing the photonic neural network architecture.

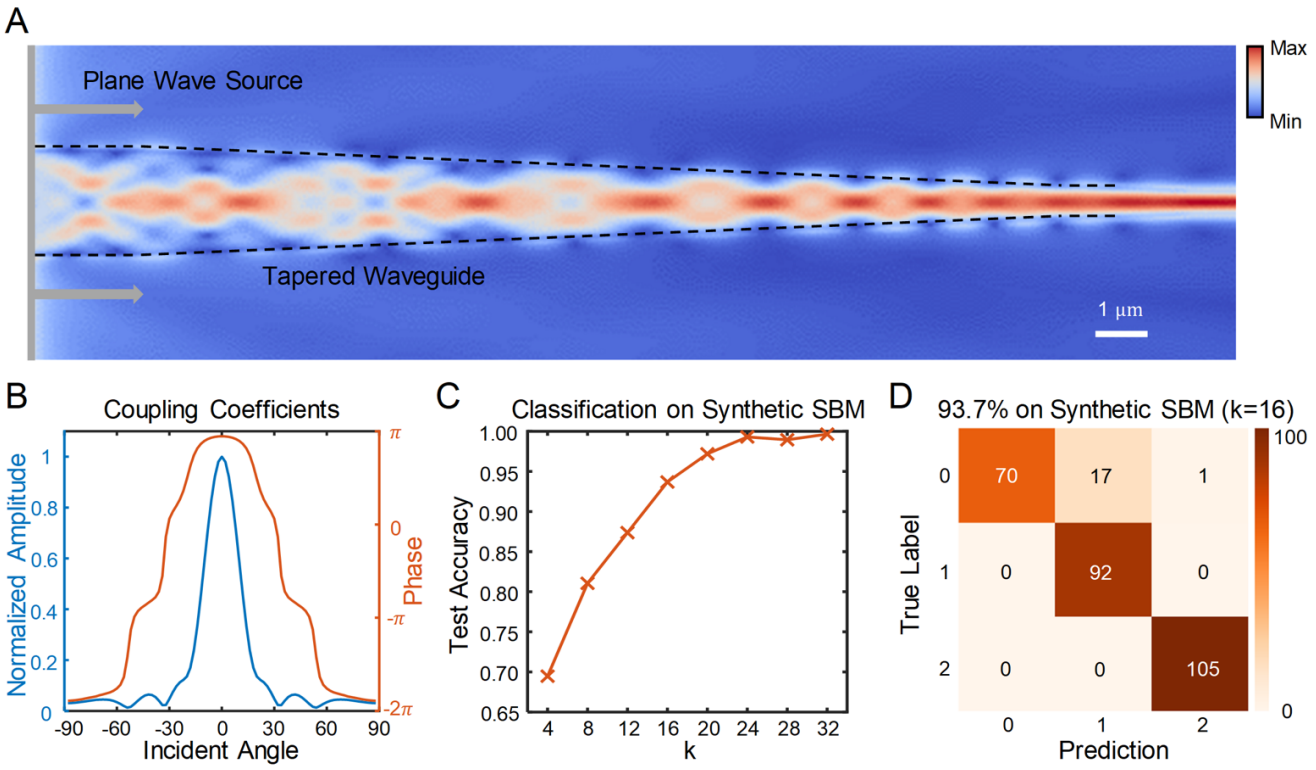

Figure S5. DPU output port with the tapered waveguide. (A) The coupling of the electric field between the plane optical wavefront and a tapered waveguide. Tapered waveguides can be used for coupling more optical energy to the output ports of integrated DPU, where the core width at the beginning is wider (i.e., 2 μm in this example) than single-mode waveguides (500 nm). (B) The normalized coupling coefficients of the tapered waveguide with respect to the incident angle of the plane wave source were obtained via FDTD. (C) Classification results of DGNN-E on the Synthetic SBM graph under different top-k neighboring node settings. Node representations are obtained via FDTD evaluations by using the DPU with tapered output waveguides in (A). The results achieve a maximum test accuracy of 99.7% with $k = 32$, which is comparable to the DPU with single-mode output waveguides in Fig. 2 of the main text. (D) Confusion matrix of the classification results with $k = 16$, corresponding to an accuracy of 93.7%.

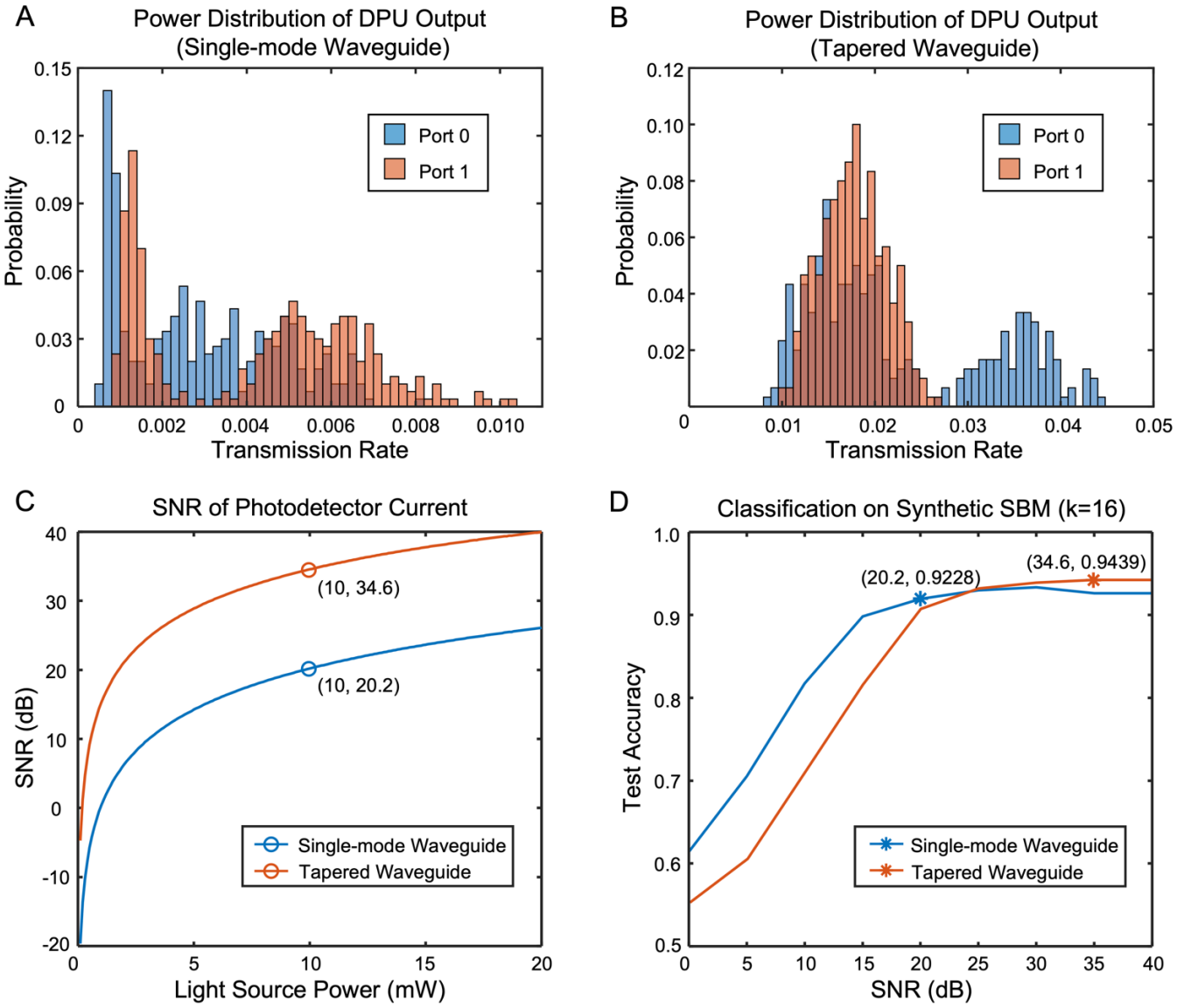

Figure S6. Performance of the DGNN-E with single-mode and tapered output waveguides. Power distributions of DPU output ports configured with single-mode (A) and tapered (B) output waveguides on the synthetic graph test nodes are obtained based on the FDTD evaluation. (C) The photocurrent SNR of classifier input signals with respect to the input light source power. (D) The classification accuracy of DGNN-E on the synthetic SBM graph with respect to the photocurrent SNR of DPU outputs.

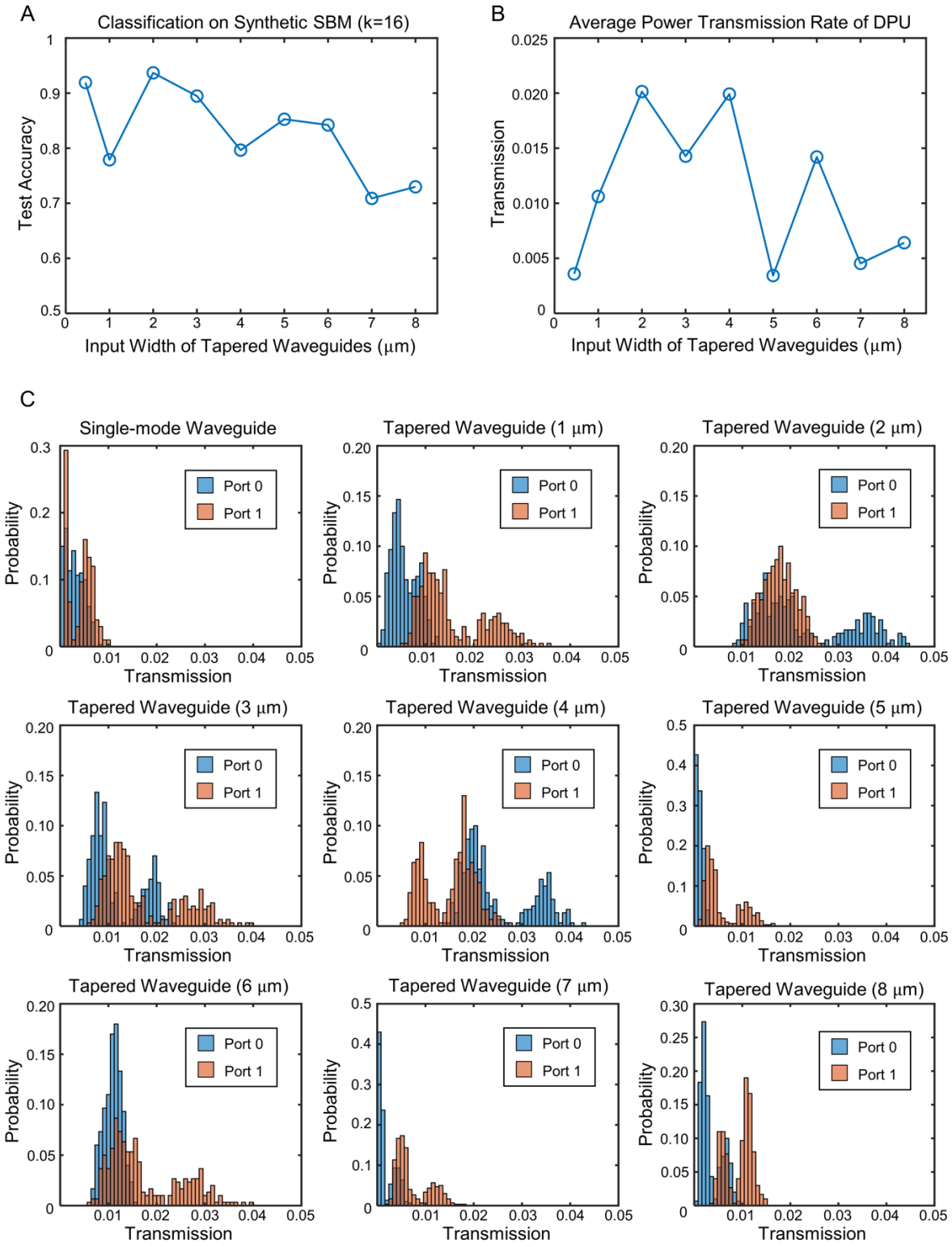

Figure S7. Optimizing the taper angle of output waveguides. The classification accuracy of DGNN on the synthetic SBM graph (A) and the averaged power transmission rate of DPU (B) with respect to the

taper angle are obtained by varying the input width of tapered waveguides under a fixed waveguide length of 20 μm. (C) The corresponding output port power distributions under different input widths of tapered waveguides. Notice that 500 nm input width corresponds to the single-mode waveguide.

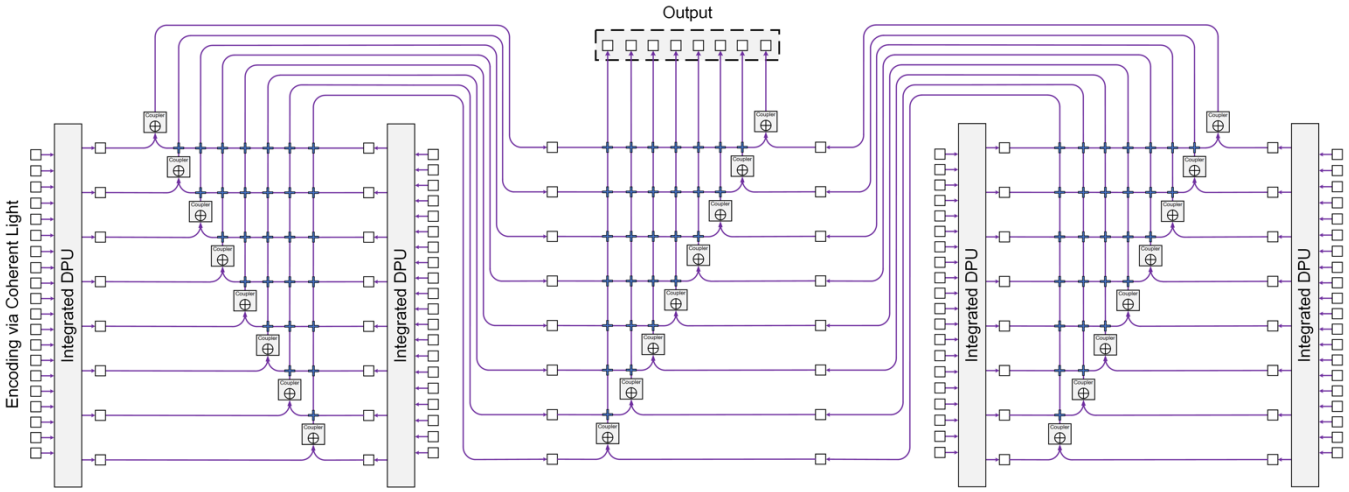

Figure S8. Scale-up the neural message dimension of the DGNN node. The high-dimensional optical neural messages of neighborhood nodes calculated from the DPU module are aggregated through the optical strip waveguide and optical Y-coupler with waveguide crossing.

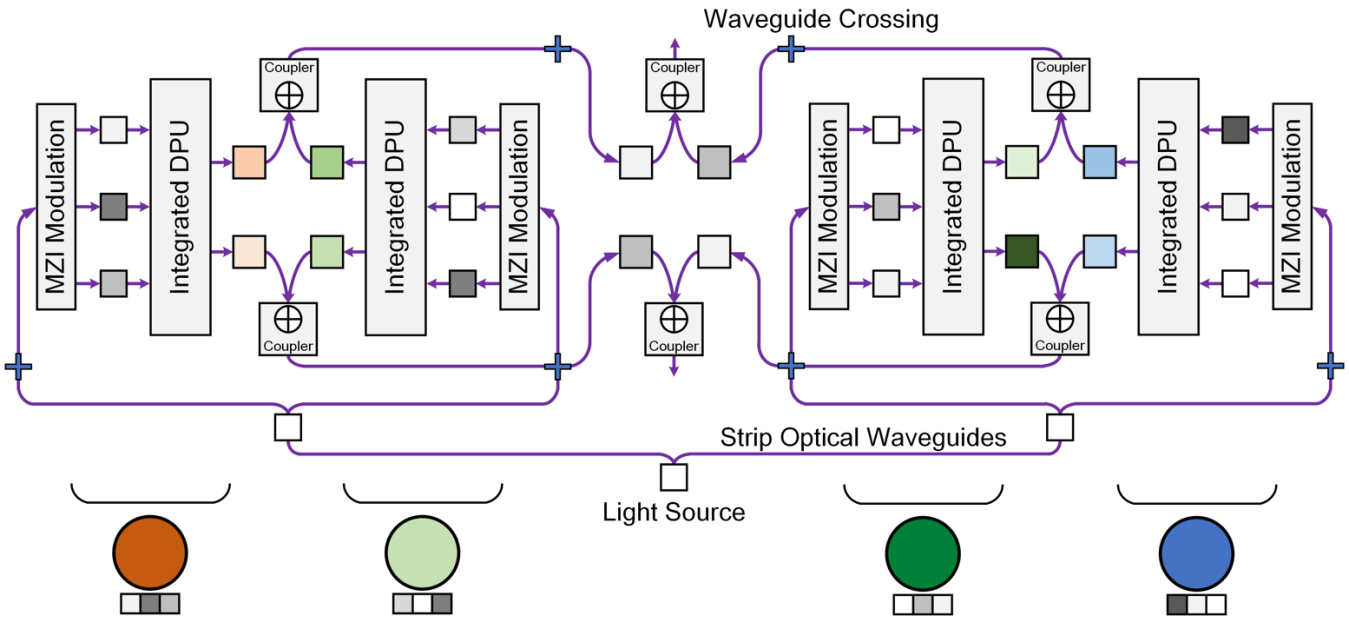

Figure S9. DPU inputs of the DGNN. The node attributes can be encoded as inputs to the DPU module by using the MZI modulators, where the coherent light source is injected through the optical strip waveguide and optical on-chip beam-splitter with waveguide crossing.

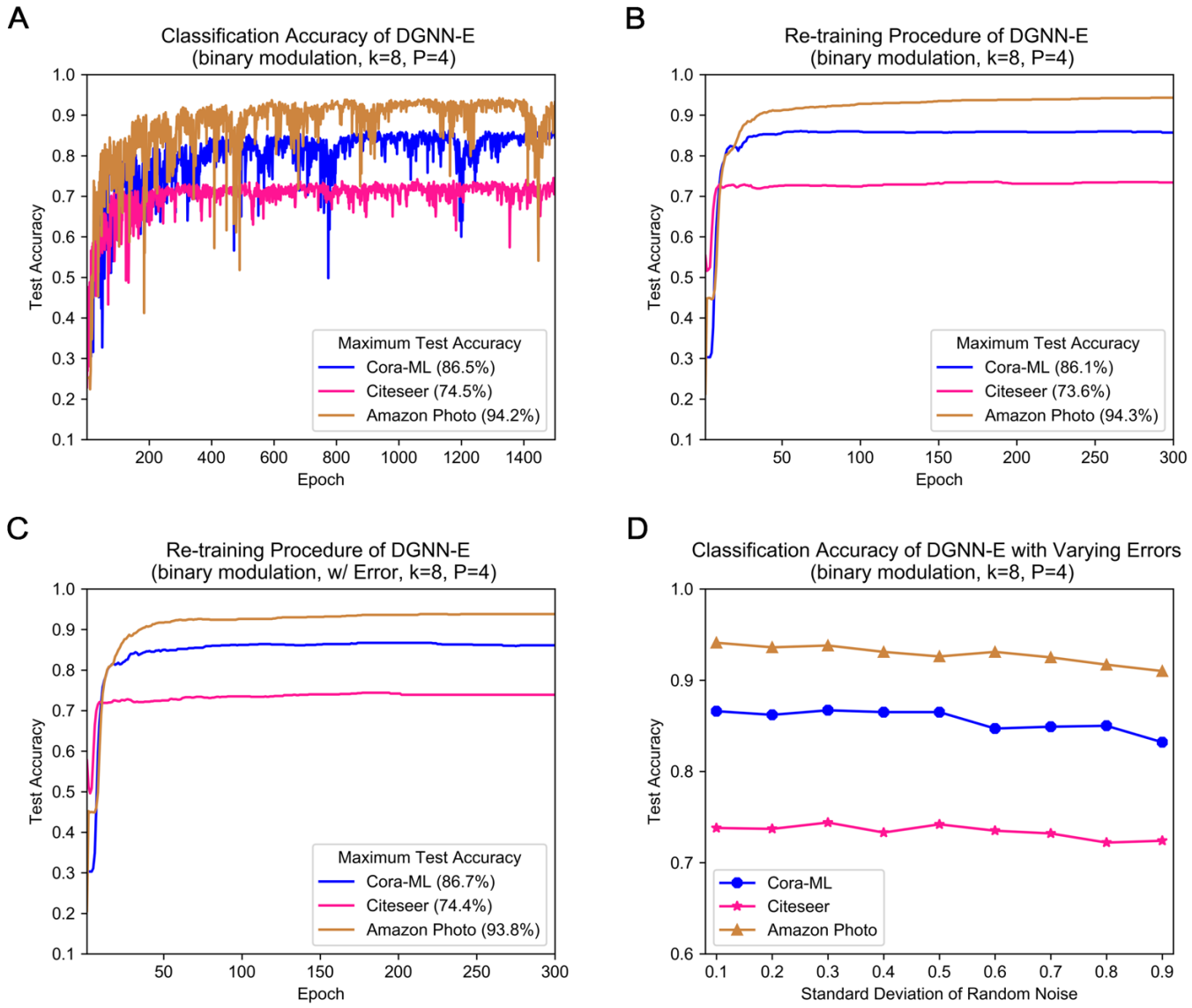

Figure S10. Training of DGNN-E with binary modulation. (A) The convergence plot of test accuracy on three benchmark databases during the initial training procedure. (B) The optical parameters of the trained DPU are fixed, and the output electronic classifier is re-trained. (C) The Gaussian random noise with a standard deviation of 0.3 is included in both the amplitude and phase modulation coefficients of diffractive layers obtained from (a), and the output electronic classifier is re-trained. (D) The test accuracy with respect to the different amounts of Gaussian noise included, with standard deviation varying from 0.1 to 0.9.

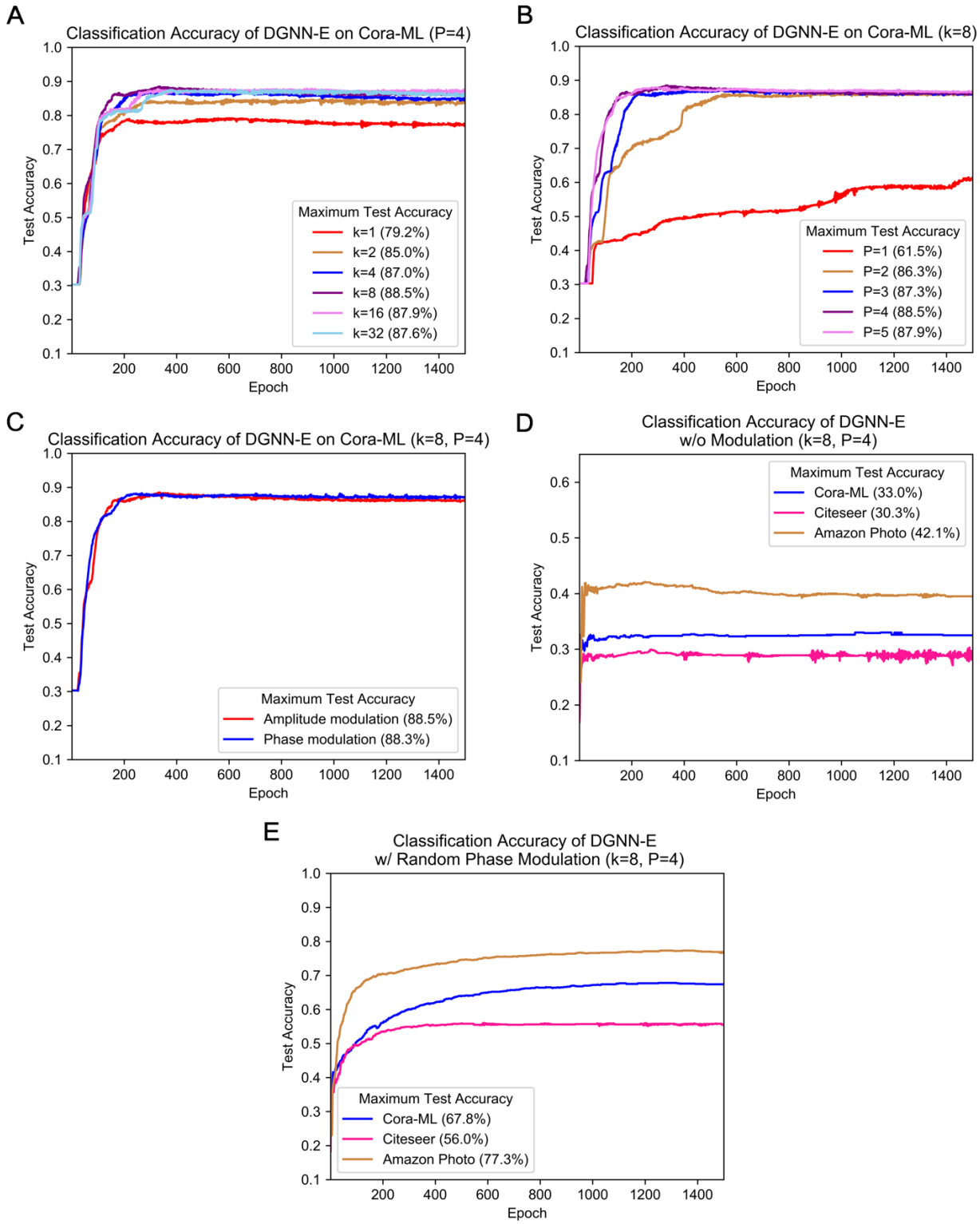

Figure S11. Ablation study of DGNN in semi-supervised node classification. (A) The performance of DGNN-E with respect to the number of neighbors selected by top-*k* personalized PageRank scores. (B)

The performance of DGNN-E with respect to the number of heads P. (C) The performance of DGNN-E by encoding the node attributes to the amplitude/phase of the coherent light. (D) The performance of DGNN-E without optical modulations in $\mathrm{MSG}(\cdot)$. (E) The performance of DGNN-E with random phase modulation in $\mathrm{MSG}(\cdot)$.

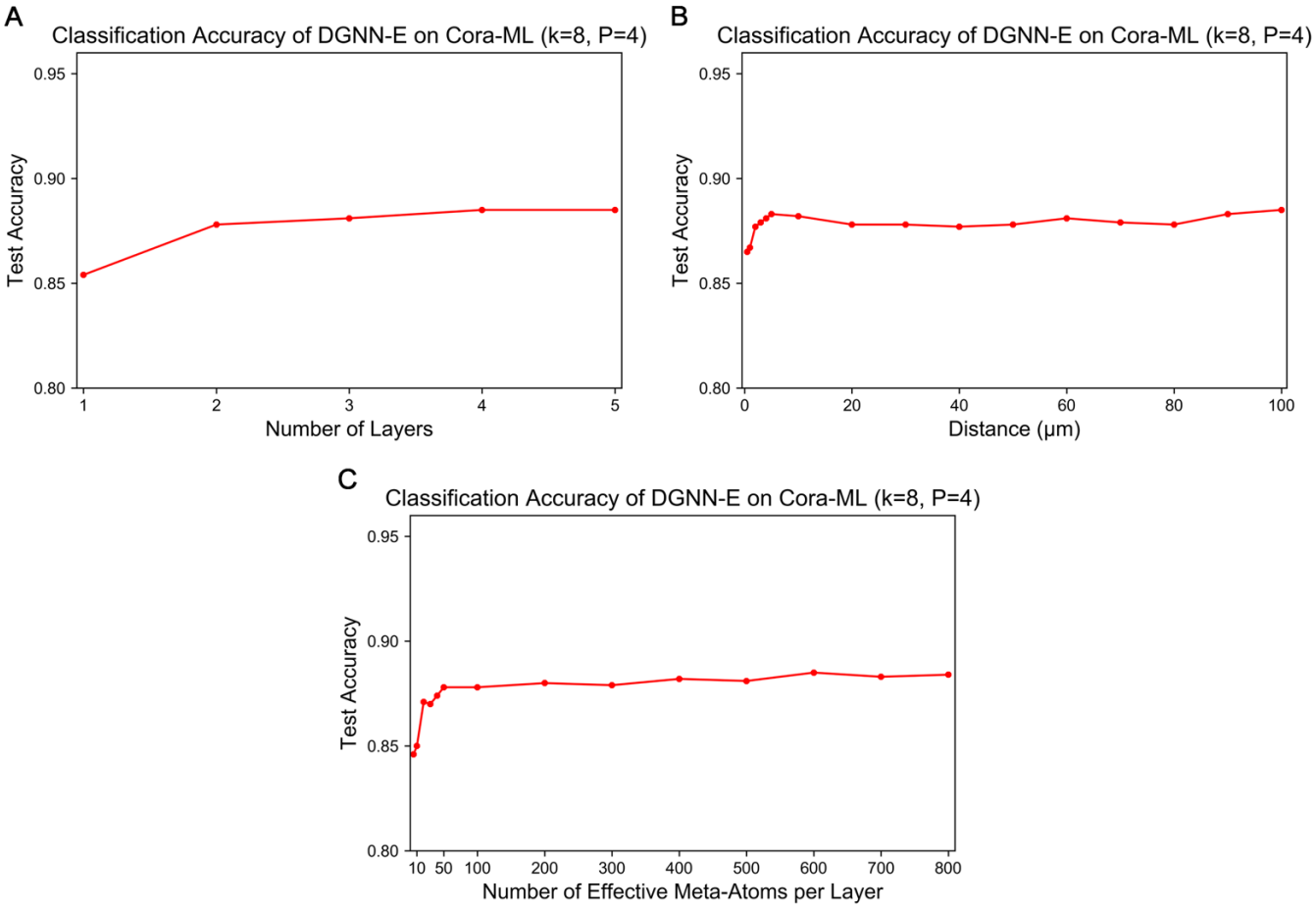

Figure S12. Ablation study of geometric parameters of DPUs. (A) The performance of DGNN-E with respect to the number of diffractive layers in DPU. (B) The performance of DGNN-E with respect to the distance between successive diffractive layers in DPU. (C) The performance of DGNN-E with respect to the number of effective meta-atoms per diffractive layer in DPU, where consecutive meta-atoms with the same parameters are considered as one effective meta-atom.

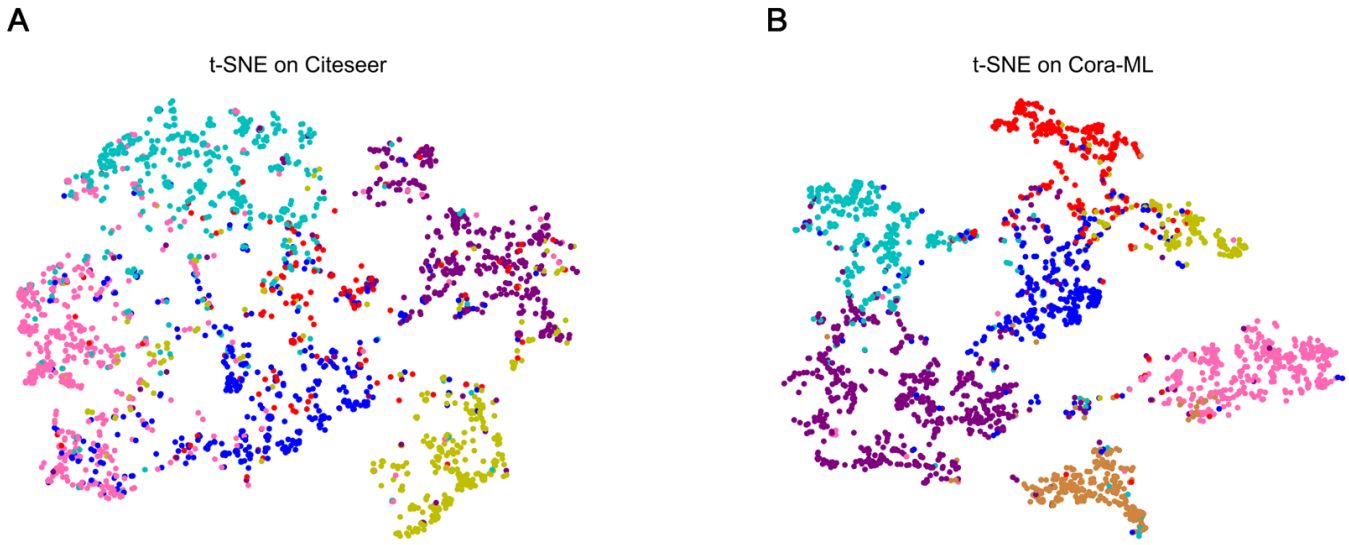

Figure S13. t-SNE visualization of node representations of DGNN-E. Extended t-SNE visualizations on Citeseer (A) and Cora-ML (B) databases in addition to Fig. 3C of the main text.

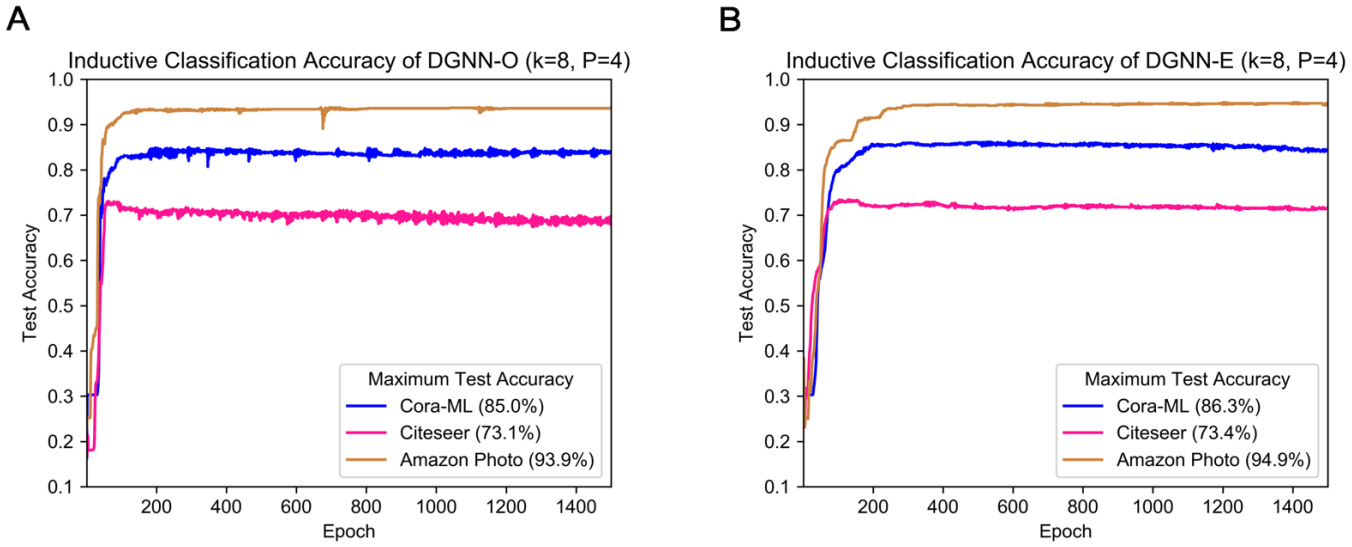

Figure S14. Inductive classification results of DGNN on three benchmark graphs. The performance of DGNN-O (A) and DGNN-E (B) architectures on the Cora-ML, Citeseer, and Amazon Photo databases are analytically evaluated by using inductive learning. The test accuracy convergence plots are shown.

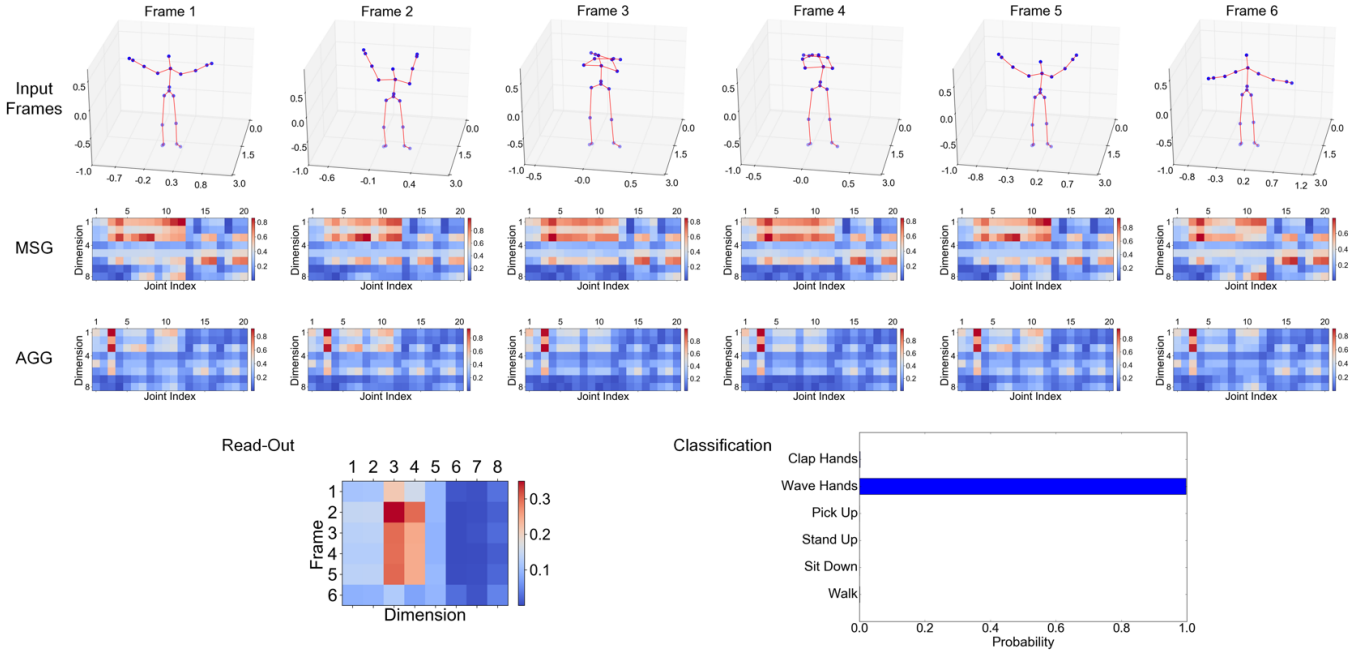

Figure S15. Extended results of DGNN on skeleton-based action recognition. A selected sub-sequence from the test set for performing the action category of wave hands is visualized. The normalized amplitude of each frame processed after optical $\mathrm{MSG}(\cdot)$, $\mathrm{AGG}(\cdot)$, the L_2-normalized intensity values after optical $\mathrm{Read\text{-}Out}(\cdot)$, and the classification result are shown.

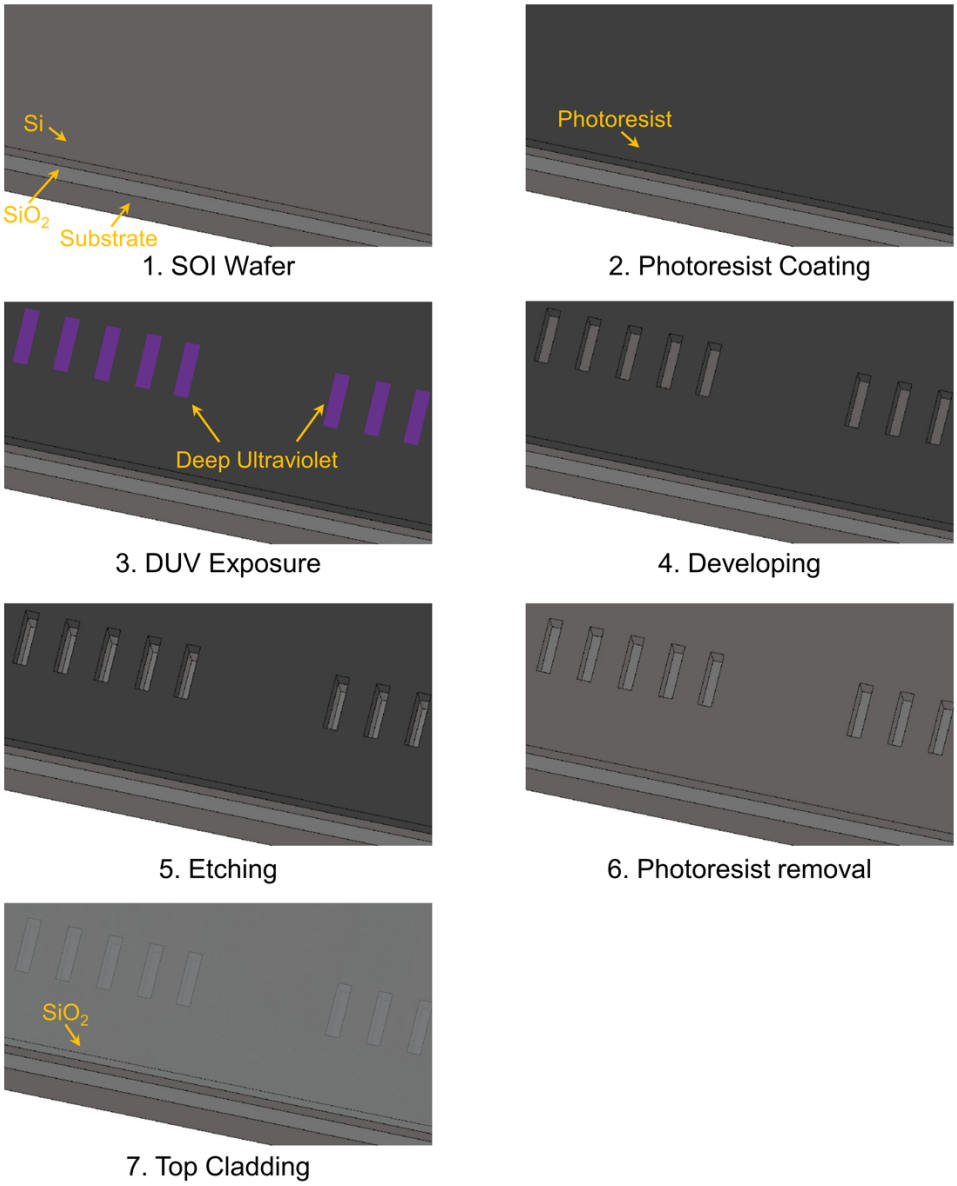

Figure S16. Schematic of the fabrication process for photonic metalines. The fabrication process of diffractive metalines can be based on silicon photonic semiconductor fabrication techniques, including the photoresist coating, deep ultraviolet (DUV) exposure, developing, etching, photoresist removal, and top cladding.

Table S1. Summary of dataset statistics. The isolated nodes and nodes without attributes are removed.

Dataset	Cora-ML	Citeseer	Amazon Photo
# Nodes	2995	3312	7535
# Edges	8158	4536	119081
# Features	2879→20	3703→20	745→20
# Classes	7	6	8

Table S2. Inductive node classification results (%) on three graph benchmark datasets. Note that the DGNN are configured with $k = 8$ and $P = 4$.

Dataset	Cora-ML	Citeseer	Amazon Photo
PCA	77.7	70.2	89.9
MLP	80.5	70.8	93.0
PPRGo-S	86.0	73.3	94.9
PPRGo-WS	86.7	75.4	95.1
DGNN-O	85.0	73.1	93.9
DGNN-E	86.3	73.4	94.9
DGNN-E (binary modulation)	86.2	73.9	94.3

Table S3. Semi-supervised node classification results (%) on the Amazon Photo dataset under different sizes of training labels.

# Labels per class	1	5	10	15	20	25
PCA	37.9	69.3	78.1	81.5	84.7	85.3
MLP	37.8	67.3	76.4	80.2	82.3	83.1
PPRGo-S	65.9	76.6	84.3	87.4	89.6	90.4
PPRGo-WS	57.7	76.5	81.6	87.2	89.3	90.6
DGNN-O	65.8	83.6	88.6	89.3	90.9	90.7
DGNN-E	58.1	77.0	86.4	88.3	90.2	90.4
DGNN-E (binary modulation)	70.6	83.1	87.7	89.3	90.9	91.1